



# Wetting controls of droplet formation in step emulsification

Maximilian L. Eggersdorfer<sup>a,1</sup>, Hansjörg Seybold<sup>b,1</sup>, Alessandro Ofner<sup>c,1</sup>, David A. Weitz<sup>a</sup>, and André R. Studart<sup>c,2</sup>

<sup>a</sup>School of Engineering and Applied Sciences, Harvard University, Cambridge, MA 02138; <sup>b</sup>Physics of Environmental Systems, Department of Environmental System Sciences, ETH Zürich, 8092 Zürich, Switzerland; and <sup>c</sup>Complex Materials, Department of Materials, ETH Zürich, 8093 Zürich, Switzerland

Edited by Howard A. Stone, Princeton University, Princeton, NJ, and approved August 8, 2018 (received for review March 1, 2018)

The formation of droplets is ubiquitous in many natural and industrial processes and has reached an unprecedented level of control with the emergence of milli- and microfluidics. Although important insight into the mechanisms of droplet formation has been gained over the past decades, a sound understanding of the physics underlying this phenomenon and the effect of the fluid's flow and wetting properties on the droplet size and production rate is still missing, especially for the widely applied method of step emulsification. In this work, we elucidate the physical controls of microdroplet formation in step emulsification by using the wetting of fluidic channels as a tunable parameter to explore a broad set of emulsification conditions. With the help of high-speed measurements, we unequivocally show that the final droplet pinch-off is triggered by a Rayleigh–Plateau-type instability. The droplet size, however, is not determined by the Rayleigh–Plateau breakup, but by the initial wetting regime, where the fluid's contact angle plays a crucial role. We develop a physical theory for the wetting process, which closely describes our experimental measurements without invoking any free fit parameter. Our theory predicts the initiation of the Rayleigh–Plateau breakup and the transition from dripping to jetting as a function of the fluid's contact angle. Additionally, the theory solves the conundrum why there is a minimal contact angle of  $\alpha = 2\pi/3 = 120^\circ$  for which droplets can form.

droplet formation | microfluidics | surface wetting | contact angle | step emulsification

Monodisperse microdroplets in designer emulsions introduce a new level of control and efficiency in many processes and applications. Examples are microreactors in chemical engineering (1), cell manipulation in biomedical systems (2, 3), and the synthesis of functional materials (4–7). Contrary to droplet makers based on flow focusing (8, 9), coflow (10–12), or T-junction approaches (13), the step emulsifiers (14–16) do not require a secondary flow to trigger the droplet breakup (14, 17, 18). Thus, such devices are easier to control, less susceptible to perturbations (19), and are more conveniently parallelized (17, 20). While the robustness and parallelization potential of these devices enable new biomedical and materials technologies, the details of the physical mechanisms controlling the droplet breakup, the influence of surface wetting on the droplet diameter, and the transition from droplet dripping to jetting are not fully understood (21–26).

Here, we show that droplet formation by step emulsification occurs through the sequential dewetting of the dispersed fluid from the nozzle walls, followed by a droplet pinch-off via a Rayleigh–Plateau-type instability. Although the Rayleigh–Plateau instability is responsible for the pinch-off, the formation of the neck and therefore the final droplet diameter is controlled by the initial wetting process, where the fluid's contact angle with the nozzle surface plays a crucial role. We develop a simple physical theory, which does not require a detailed knowledge of the hydrodynamics, but nonetheless accurately predicts the transition from dripping to jetting as a function of a rescaled capillary number.

To understand the breakup of a dispersed fluid into droplets, we combine theoretical modeling, microfluidic experiments, and

3D numerical simulations (*SI Appendix*). In a step emulsification device, droplets are created by injecting the dispersed phase through a shallow wedge-shaped channel into a reservoir which is deeper than the final droplet diameter and contains an immiscible continuous phase (Fig. 1, overview). At the beginning of this process, the dispersed phase forms a tongue inside the nozzle. Fig. 1 (experiment, top) shows microscope images of the experiment together with the corresponding cross-sections through the horizontal midplane of the numerical simulations, Fig. 1 (simulations, top). Once the tongue reaches the end of the nozzle, it expands into the reservoir forming a bulb (Fig. 1A, *i*). Initially, this bulb remains connected to the main thread in the nozzle through a neck (Fig. 1A, *ii*). A schematic vertical cross-section through the neck is shown in Fig. 1 (front). The width of the neck continuously decreases (Fig. 1A, *iii*) until the thread finally ruptures at  $t = t_b$ , forming a droplet (Fig. 1A, *iv*). This flow regime of monodisperse droplet formation is called dripping. If the flow rate is too high the thread does not rupture, resulting in jetting of the dispersed phase (Fig. 1B, *i* and *ii*). In this regime, droplets are sheared off the bulb in an uncontrolled way, resulting in droplets of varying sizes.

The formation of the bulb is driven by the difference in Laplace pressure between the highly curved liquid interface inside the shallow channel and the less-curved interface generated as the dispersed phase expands into a spherical shape within the deeper reservoir (23). Fig. 2A shows the pressure profile along the central axis of the nozzle extracted from 3D numerical simulations. The pressure drop between the neck,  $p_n$ , and the

## Significance

Step emulsification is one of the few methods that enables upscaled production of droplets with a monodispersity desired for many industrial processes. However, the physical mechanisms of the droplet formation process are poorly understood. We study the droplet breakup by experiments and simulations and find a simple theory predicting the transition from dripping to jetting and the minimal contact angle of  $\alpha = 2\pi/3 = 120^\circ$  for which droplets form. These results have important consequences for the development and design of novel microfluidic systems and reactors that address the growing demand for tools to manipulate fluids at the submillimeter scale.

Author contributions: M.L.E., H.J.S., and A.O. designed the project; M.L.E. developed the physical model; H.J.S. performed the numerical simulations; A.O. carried out the experiments; M.L.E., H.J.S., and A.O. analyzed the data and synthesized the results; D.A.W. and A.R.S. contributed to the discussion and interpretation of the data; and M.L.E., H.J.S., A.O., D.A.W., and A.R.S. wrote the paper.

The authors declare no conflict of interest.

This article is a PNAS Direct Submission.

Published under the PNAS license.

<sup>1</sup>M.L.E., H.J.S., and A.O. contributed equally to this work.

<sup>2</sup>To whom correspondence should be addressed. Email: andre.studart@mat.ethz.ch.

This article contains supporting information online at [www.pnas.org/lookup/suppl/doi:10.1073/pnas.1803644115/-DCSupplemental](http://www.pnas.org/lookup/suppl/doi:10.1073/pnas.1803644115/-DCSupplemental).

Published online September 5, 2018.

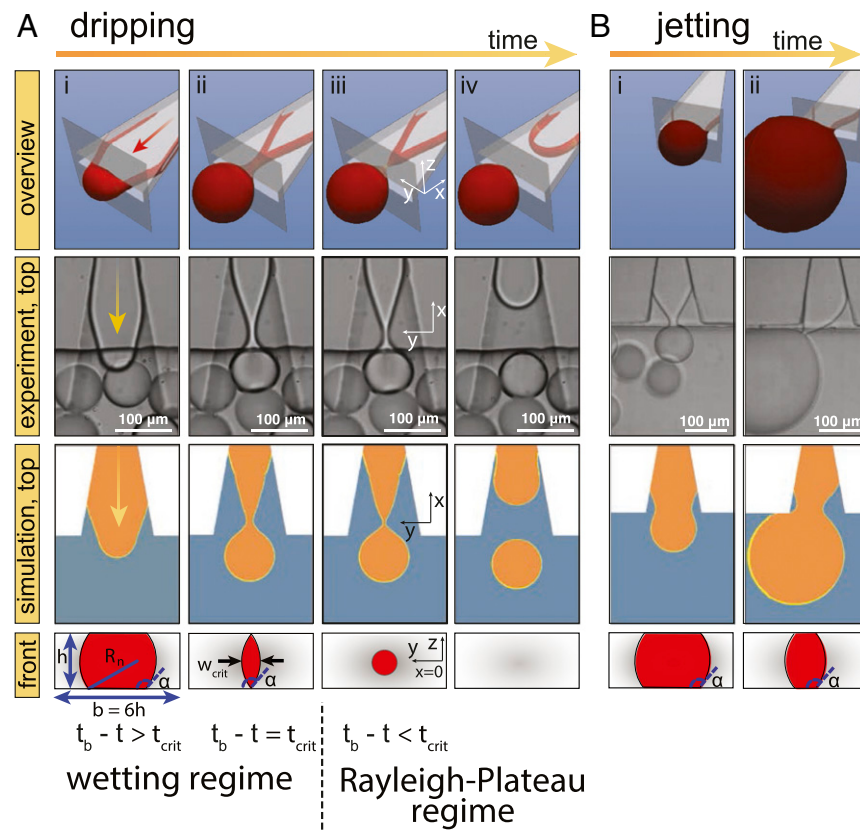


**Fig. 1.** (A) Droplet formation in a step emulsification device at different times (*A*, *i*-*iv*). Perspective views of the 3D numerical simulations are shown in the top row (overview) together with the corresponding experiments and horizontal cross-sections below. The dispersed phase is squeezed through a shallow channel forming a tongue. The dispersed thread expands into a bulb upon entering the deeper reservoir until the drop pinches off at  $t = t_b$ . The capillary number in both experiment and simulation is approximately  $Ca \sim 0.006$  and the contact angle is  $\alpha \sim 150^\circ$  in both cases. (B) For high flow rates, the thread remains stable and the bulb continues to grow until it is finally sheared off in the reservoir. The capillary number for the experiment is  $Ca = 0.016$  and for the simulation it is approximately  $Ca = 0.1$ , which explains the wider neck in the numerical simulation compared with experiment. The front panels show a schematic view of the cross-section through the neck. The thread detaches from the top and bottom of the nozzle at time  $t_b - t = t_{crit}$  resulting in a critical neck width  $w_{crit}$ . After the neck is fully disconnected from the nozzle walls the free thread collapses in a Rayleigh–Plateau-type breakup.

bulb,  $p_d$ , can be expressed by the difference in curvature of the fluid–fluid interface (27):

$$\Delta p = p_n - p_d = \gamma(\kappa_n - \kappa_d), \quad [1]$$

where the off-plane curvature of the neck,  $\kappa_n$ , is fixed by the channel height,  $h$ , and the contact angle (23, 28),  $\alpha$ , according to the relation (*SI Appendix*)

$$\kappa_n = 1/R_n = -2 \cos(\alpha)/h. \quad [2]$$

The in-plane curvature of the neck is significantly lower than the off-plane curvature and is therefore neglected here (*SI Appendix*). The curvature of the bulb  $\kappa_d = 2/R_d$  decreases during the filling process, reducing the pressure  $p_d$ . Consequently, the pressure drop  $\Delta p$  rises and the flow  $Q_{out}$  from the neck into the bulb increases. When  $Q_{out}$  surpasses the flow into the nozzle  $Q_{in}$ , the neck width  $w$  shrinks until it reaches a critical value of

$$w_{crit} = 2R_n[1-\cos(\alpha - \pi/2)] = \frac{h}{\cos \alpha} \cdot [\sin \alpha - 1]. \quad [3]$$

This critical width corresponds to the minimum achievable width of the thread that still satisfies the surface wetting constraint (Eq. 2) and can be derived by simple geometric arguments (Fig. 1*A*, *ii*, front and *SI Appendix*). Once the thread detaches from the

nozzle walls, the neck becomes unstable and rapidly collapses (Fig. 1*A*, *iii*).

To investigate the dynamics of the collapse, we record the evolution of the fluid interface with up to 200,000 frames per second and compare the theoretical prediction of  $w_{crit}$  (Eq. 3) with experimental results and numerical simulations (Fig. 2*B* and *C*). Fig. 2*B* shows how the neck width  $w$  decreases as a function of time relative to the breakup time,  $t_b$ . Red squares indicate the experimental data and the corresponding simulations are marked in blue. In both cases the contact angle is around  $\alpha = 150^\circ$ . The power-law behavior of the Rayleigh–Plateau regime can be clearly distinguished from the initial wetting regime. The instability is triggered when the neck detaches from the nozzle walls, forming a free thread at a neck width  $w_{crit}$  ( $\alpha = 150^\circ$ )  $\sim 0.6 h$ , consistent with Eq. 3. The fact that the initiation of the breakup coincides with the predicted neck width of  $w_{crit}$  for both experiment and simulation (Fig. 2*B*, orange arrow) strongly supports our simple model. Experiments and simulations performed for different contact angles show that  $w_{crit}$  can be well described by the proposed theory (Fig. 2*C*).

The power-law scaling of the instability indicates a Rayleigh–Plateau-type breakup, where the neck width  $w \sim |t_b - t|^\xi$  follows a finite time singularity with exponent  $\xi = 1/2$ . In the classic, inertia-dominated Rayleigh–Plateau breakup of a free liquid thread, the scaling exponent of the power-law collapse is 2/3

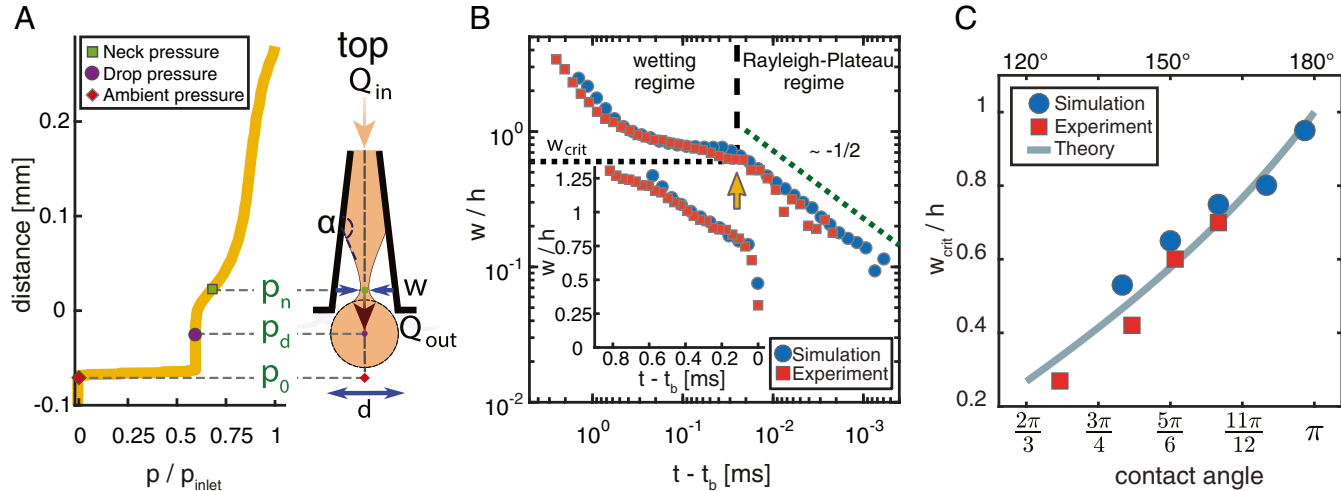


**Fig. 2.** (A) Simulated pressure profile along the central axis of the dispersed fluid thread (Left) together with a schematic view of the nozzle thread system (Right). The pressure gradient between the neck,  $p_n$ , and the bulb,  $p_d$ , is driving the initial growth of the bulb until the thread detaches from the nozzle walls. All pressure values are normalized by the pressure at the inlet and the ambient pressure  $p_0$  is defined as zero. (B) Scaling of the normalized neck width,  $w/h$ , as a function of time. Experiments (red squares) and simulation (blue circles) have comparable capillary number and the contact angle is  $\alpha \sim 150^\circ$  in both cases. The power-law behavior of the Rayleigh-Plateau-type instability is triggered at a critical neck width  $w_{crit}$  ( $\alpha = 150^\circ$ )  $\sim 0.6$  h (orange arrow). During the initial wetting phase the neck width decreases linearly with time (Inset). (C) Critical neck width  $w_{crit}$  as function of the wetting contact angle  $\alpha$ . Blue circles represent results from numerical simulations and red squares indicate experimental measurements. The gray solid line is the theoretical prediction of  $w_{crit}$  by Eq. 3.

(29, 30). The difference between the breakup in the nozzle and the classical Rayleigh-Plateau scaling suggests that both viscous and inertial forces may affect the final stage of the breakup (31).

While the Rayleigh-Plateau-type instability is responsible for the final pinch-off, the growth of the bulb and therefore the final droplet size is dominated by the wetting regime. Fig. 2B (Inset) shows the same data as in the main figure but on a linear scale. In the wetting regime, the neck width decreases linearly with time analogous to the thinning of a viscous thread (31). This supports the assumption that the filling of the bulb is controlled by an equilibrium between viscous forces and surface tension (17, 32).

Next, we examine the effect of surface wetting on the dripping-to-jetting transition of the step emulsification process. This transition is highly relevant for practical applications, since it determines the maximum throughput rate that can be achieved during the production of monodisperse droplets by dripping (26, 33). To trigger the formation of droplets in a step emulsification device, the nozzle must be depleted faster than the thread is refilled ( $Q_{in} < Q_{out}$ ) resulting in a decreasing neck width  $w$  over time. If the flow into the nozzle balances the outflow,  $Q_{in} = Q_{out}$ , before reaching the critical width  $w_{crit}$  (Eq. 3), the neck cannot shrink sufficiently to trigger the Rayleigh-Plateau breakup. In this case, the bulb continues to grow without forming a droplet, resulting in jetting of the dispersed phase (Fig. 1B). To identify the parameters that control this transition, we estimate and compare the magnitudes of  $Q_{in}$  and  $Q_{out}$  at the critical moment when the thread reaches the minimum possible neck width  $w_{crit}$  (for details see *SI Appendix*). In a first approximation, the filling of the bulb at this point in time can be described by the Hagen-Poiseuille equation (34),  $p_n - p_d = R_H Q_{out}$ . Here,  $R_H$  is a hydrodynamic resistance determined by the geometry of the thread inside the nozzle (*SI Appendix*, Fig. S1). The filling of the nozzle is described in terms of the dimensionless capillary number,  $Ca = (Q_{in}\eta)/(h^2\gamma)$ , with  $\eta$  being the viscosity of the dispersed phase. Considering that  $Q_{in} < Q_{out}$  is necessary to ensure that the neck detaches and droplets are formed by dripping, the condition for the

transition from dripping to jetting can be expressed as a constraint on the capillary number (*SI Appendix*):

$$Ca_{crit} = \frac{\pi}{128} [2 \cos(\pi - \alpha) - 1]. \quad [4]$$

To test this prediction, we perform experiments and 3D numerical simulations for various combinations of contact angles at different capillary numbers (Fig. 3A). The variation of the contact angles over a wide range of values is possible by taking advantage of the chemical robustness and surface tunability of glass (20). Contrary to polymeric microfluidic devices, such as polydimethylsiloxane (PDMS) or poly(methyl methacrylate) (PMMA), glass devices do not only allow one to use almost any solvent, but also enable a wide range of surface functionalizations to modify the contact angle without the need to change the solvents (20). This flexibility of glass devices opens the possibility for a systematic investigation of the physics underlying the step emulsification process and provides an additional control parameter for the high-throughput formation of designer droplets (17, 20) (*SI Appendix*). The comparison of the theoretical prediction (orange curve, Fig. 3A) with our data shows that the critical capillary number  $Ca_{crit}$  given by Eq. 4 describes remarkably well the dripping-to-jetting transition for both experiments (squares) and numerical calculations (circles). It is important to note that the flow rates of the experiments are determined by averaging droplet volumes over several dripping events within a given time span. Hence the critical capillary number for the jetting transition can only be estimated experimentally with some uncertainty. This explains some of the inconsistencies between the experimental data and the theoretical prediction close to the jetting transition.

Another direct consequence of our theory (Eq. 4) is the explanation of a lower bound for the contact angle to form droplets by dripping, namely  $\alpha > 2\pi/3 = 120^\circ$ . This threshold has been observed in our experiment and others (35). For contact angles smaller than  $120^\circ$  the pressure drop between the neck and the bulb becomes zero, thus removing the driving force for droplet formation by dripping. Fig. 3B demonstrates this wetting angle threshold by simply tuning the roughness of the nozzle glass

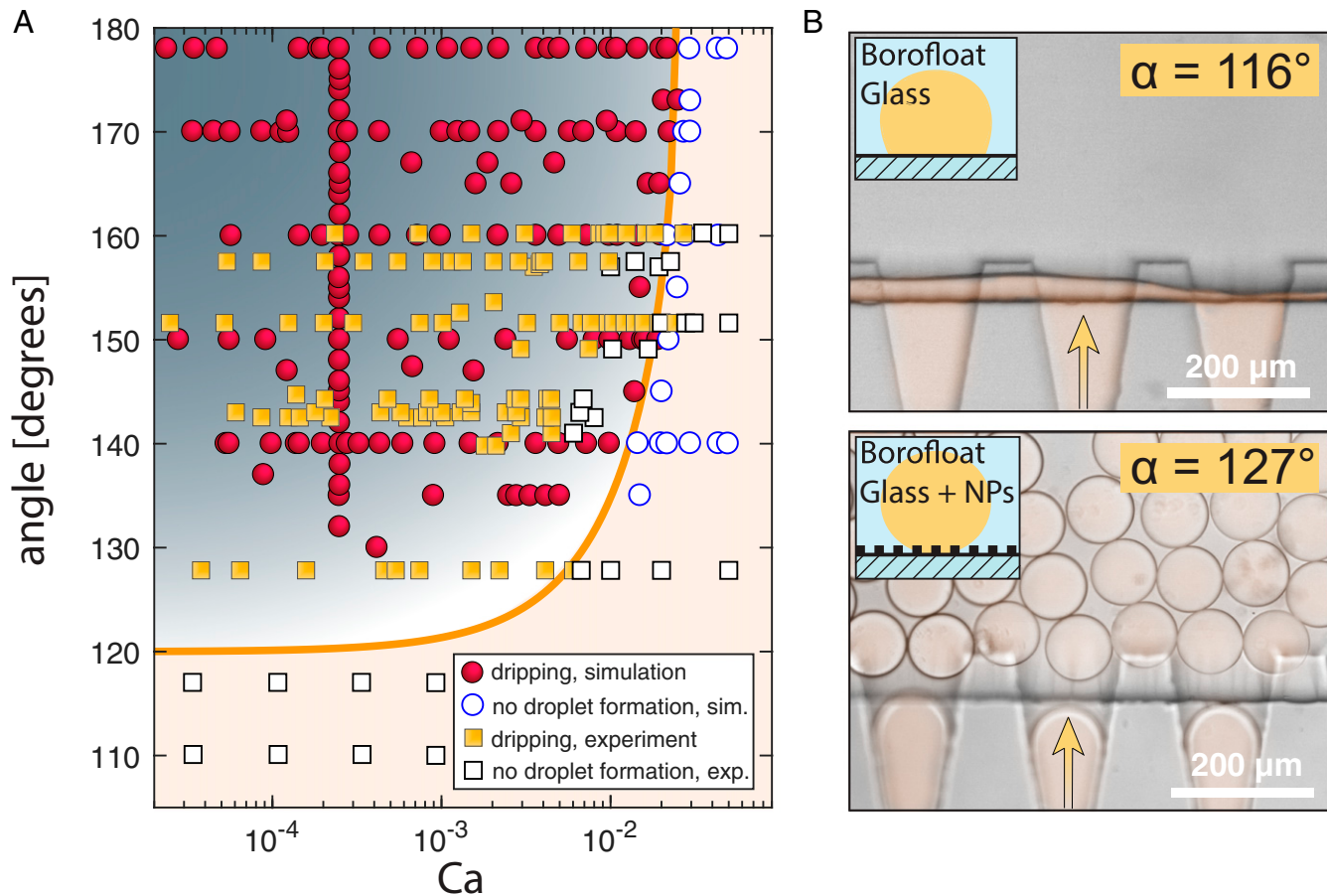


**Fig. 3.** (A) Phase diagram for the transition from dripping (droplet formation) to jetting (continuous flow) as a function of surface wetting and capillary number. The orange line denotes the theoretical prediction. Experiments are marked with squares and circles represent simulations. Open symbols stand for no droplet formation and solid symbols mark dripping. Below the critical contact angle of  $\alpha = 120^\circ$  no droplets form for any capillary number. The darker the background the smaller the droplet diameter. (B) Surface functionalization can be used to increase the contact angle above  $120^\circ$  to emulsify systems which cannot be emulsified otherwise due to the wetting constraint, Eq. 4: Hexane injected in water without surface functionalization (*Top*) and with silica nanoparticle coating (*Bottom*). The flow direction in the nozzle is indicated by a yellow arrow and the hexane phase is marked in light orange.

walls. On a smooth glass surface, hexane forms a contact angle of  $116^\circ$  with water which is below the  $120^\circ$  threshold, and thus emulsification is not observed, Fig. 3B (*Top*). However, the nozzle surface can be roughened through silica nanoparticle coating which increases the contact angle above  $120^\circ$ . This simple change enables the creation of monodisperse droplets that would not form otherwise (Fig. 3B, *Bottom*).

Both experiments and simulations also indicate a clear dependence of the droplet size on the contact angle (Fig. 4A), while for small capillary numbers the droplet size is independent of the applied flow rates (Fig. 4B). The scaling of the droplet size with contact angle for small capillary numbers can be derived by combining Eqs. 1 and 2 to determine the relative pressure drop  $\Delta p/p_d = [d \cos(\pi - \alpha)/2h - 1]$  between the neck and the bulb. During the entire dewetting process this pressure difference drives the motion of the thread and remains relatively low ( $\sim 10^{-3}$ , *SI Appendix*, Fig. S4). Thus, in a first approximation  $\Delta p/p_d$  can be neglected and the droplet diameter,  $d$ , scales as (*SI Appendix*)

$$d \approx h/\cos(\pi - \alpha). \quad [5]$$

A similar dependence on the contact angle can be found if an energy balance approach similar to that proposed by Li et al. (16) is used to establish a lower bound for  $d$  (*SI Appendix*).

We evaluate the validity of this scaling relation by measuring the droplet diameter in the dripping regime for low capillary numbers ( $Ca < 3.5 \times 10^{-4}$ ) as a function of the contact angle (Fig. 4C). Indeed, the droplet size is found to be well described by the scaling relation proposed by Eq. 5. The blue solid line marks the minimal drop diameter predicted by the energy balance approach (*SI Appendix*) and the dashed line fits the proportionality from Eq. 5 to our data.

The scaling relation of Eq. 5 is only valid at low capillary numbers, where the droplet diameter is controlled by the contact angle independent of the applied flow rate. When approaching the jetting transition, the droplet size rapidly grows beyond the values expected at lower capillary numbers (Fig. 4B). Indeed, the largest droplet diameters in Fig. 4B mark the transition between droplet formation by dripping and jetting. Rescaling the capillary number with the critical value  $Ca_{crit}$  (Eq. 4) collapses the location of the dripping-to-jetting transition to a constant,  $Ca/Ca_{crit} = 1$ . Using additionally the scaling of the droplet diameter with  $\alpha$  (Eq. 5), a single master curve for the droplet size as a function of  $Ca$  is obtained (Fig. 4D). With this collapse, our model can be used to describe the effect of the wetting angle on both the droplet diameter and the dripping-to-jetting transition for a wide range of experimental conditions.

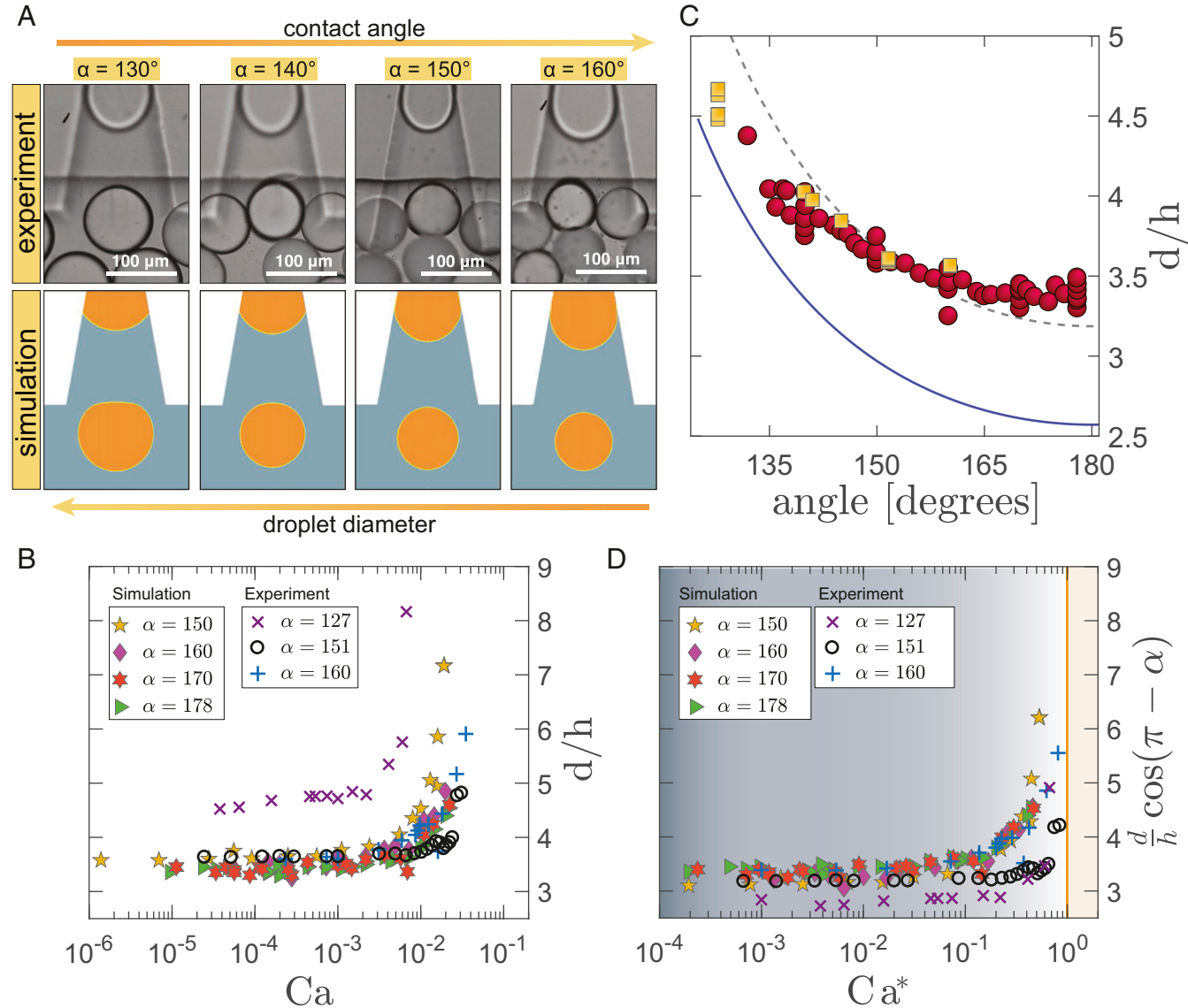


**Fig. 4.** (A) Droplet formation for contact angles between  $130^\circ$  and  $160^\circ$  in the dripping regime. With increasing contact angles, the drop diameter decreases. (B) The droplet diameter as a function of capillary number. For small capillary numbers the droplet diameter is independent of the applied flow rate. (C) The droplet diameter as function of contact angle  $\alpha$  for experiments (squares) and simulations (circles) in the limit of low capillary numbers ( $Ca < 3.5 \times 10^{-4}$ ). The theoretical prediction of the minimal droplet diameter for vanishing capillary number is plotted by a solid blue line. The influence of viscosity ratio can be accounted for by rescaling the theoretical relation (dashed lines). (D) Rescaling droplet diameter and capillary number with the wetting angle allows one to collapse all data onto a single master curve.

Our results demonstrate that controlling the wetting conditions during droplet formation not only allows a precise manipulation of the droplet diameter, but also the emulsification of fluids. Additionally, we show that the throughput of microfluidic droplet makers can be enhanced considerably by increasing the surface wetting angle. Augmenting for example the contact angle of a droplet maker with hexadecane and water by only  $10^\circ$  almost doubles its production rate. These findings greatly aid the development and design of novel microfluidic systems and reactors that address the growing demand for tools to manipulate fluids

at the submillimeter scale in chemical engineering (1, 36) and biological and medical research (2–5).

**ACKNOWLEDGMENTS.** We thank Iacopo Mattich for his help with glass surface treatment, and Patrick Rühs for fruitful discussions. The glass devices were produced at the ETH center for micro- and nanoscience, FIRST. This work was partly supported by the Swiss National Science Foundation through the National Centre of Competence in Research Bio-Inspired Materials. D.A.W. acknowledges financial support from National Science Foundation Grant DMR-1708729, Harvard Materials Research Science and Engineering Center Grant NSF DMR-1420570, and National Institutes of Health Grant R01EB023287.

1. Jensen KF (2001) Microreaction engineering—is small better? *Chem Eng Sci* 56: 293–303.
2. Whitesides GM (2006) The origins and the future of microfluidics. *Nature* 442: 368–373.
3. Sackmann EK, Fulton AL, Beebe DJ (2014) The present and future role of microfluidics in biomedical research. *Nature* 507:181–189.
4. DeMello AJ (2006) Control and detection of chemical reactions in microfluidic systems. *Nature* 442:394–402.
5. Elvira KS, Casadevall i Solvas X, Wootton RCR, deMello AJ (2013) The past, present and potential for microfluidic reactor technology in chemical synthesis. *Nat Chem* 5:905–915.
6. Studart AR, et al. (2011) Hierarchical porous materials made by drying complex suspensions. *Langmuir* 27:955–964.

7. Holtze C (2013) Large-scale droplet production in microfluidic devices—An industrial perspective. *J Phys D Appl Phys* 46:114008–114010.
8. Utada AS, et al. (2005) Monodisperse double emulsions generated from a microcapillary device. *Science* 308:537–541.
9. Hashimoto M, et al. (2008) Formation of bubbles and droplets in parallel, coupled flow-focusing geometries. *Small* 4:1795–1805.
10. Cohen C, et al. (2014) Parallelised production of fine and calibrated emulsions by coupling flow-focusing technique and partial wetting phenomenon. *Microfluid Nanofluidics* 17:959–966.
11. Priest C, Herminghaus S, Seemann R (2006) Controlled electrocoalescence in microfluidics: Targeting a single lamella. *Appl Phys Lett* 89:134101–134104.
12. Malloggi F, et al. (2010) Monodisperse colloids synthesized with nanofluidic technology. *Langmuir* 26:2369–2373.
13. Nisisako T, Ando T, Hatsuzawa T (2012) High-volume production of single and compound emulsions in a microfluidic parallelization arrangement coupled with coaxial annular world-to-chip interfaces. *Lab Chip* 12:3426–3435.
14. Kawakatsu T, Kikuchi Y, Nakajima M (1997) Regular-sized cell creation in microchannel emulsification by visual microprocessing method. *J Am Oil Chem Soc* 74: 317–321.
15. Sugiura S, Nakajima M, Seki M (2002) Prediction of droplet diameter for microchannel emulsification. *Langmuir* 18:3854–3859.
16. Li Z, Leshansky AM, Metais S, Pismen LM, Tabeling P (2015) Step-emulsification in a microfluidic device. *Lab Chip* 15:1023–1031, and erratum (2015) 15:3095.
17. Amstad E, et al. (2016) Robust scalable high throughput production of monodisperse drops. *Lab Chip* 16:4163–4172.
18. Sugiura S, Nakajima M, Iwamoto S, Seki M (2001) Interfacial tension driven monodispersed droplet formation from microfabricated channel array. *Langmuir* 17: 5562–5566.
19. Schroen K, Bliznyuk O, Muijwijk K, Sahin S, Berton-Carabin CC (2015) Microfluidic emulsification devices: From micrometer insights to large-scale food emulsion production. *Curr Opin Food Sci* 3:33–40.
20. Ofner A, et al. (2016) High-throughput step emulsification for the production of functional materials using a glass microfluidic device. *Macromol Chem Phys* 218: 1600472.
21. Nakajima M (2017) Comment on “Robust scalable high throughput production of monodisperse drops” by E. Amstad, M. Chemama, M. Eggersdorfer, L. R. Arriaga, M. P. Brenner and D. A. Weitz, *Lab Chip*, 2016, 16, 4163. *Lab Chip* 17:2330–2331.
22. Dangla R, Fradet E, Lopez Y, Baroud CN (2013) The physical mechanisms of step emulsification. *J Phys D Appl Phys* 46:114003–114009.
23. Dangla R, Kayi SC, Baroud CN (2013) Droplet microfluidics driven by gradients of confinement. *Proc Natl Acad Sci USA* 110:853–858.
24. Eggersdorfer ML, et al. (2017) Tandem emulsification for high-throughput production of double emulsions. *Lab Chip* 17:936–942.
25. Sugiura S, Nakajima M, Oda T, Satake M, Seki M (2004) Effect of interfacial tension on the dynamic behavior of droplet formation during microchannel emulsification. *J Colloid Interface Sci* 269:178–185.
26. Mittal N, Cohen C, Bibette J, Bremond N (2014) Dynamics of step-emulsification: From a single to a collection of emulsion droplet generators. *Phys Fluids* 26:082109.
27. Young T (1805) III. An essay on the cohesion of fluids. *Philos Trans R Soc London* 95: 65–87.
28. van Dijke K, de Ruiter R, Schroen K, Boom R (2010) The mechanism of droplet formation in microfluidic EDGE systems. *Soft Matter* 6:321–330.
29. Castrejón-Pita JR, et al. (2015) Plethora of transitions during breakup of liquid filaments. *Proc Natl Acad Sci USA* 112:4582–4587.
30. Lord Rayleigh FRS (1878) On the instability of jets. *Proc Lond Math Soc* s1-10:4–14.
31. McKinley GH (2005) Visco-elasto-capillary thinning and break-up of complex fluids. *Rheol Rev*, 2005:1–48.
32. Rayner M, Trägårdh G, Trägårdh C, Dejmek P (2004) Using the surface evolver to model droplet formation processes in membrane emulsification. *J Colloid Interface Sci* 279:175–185.
33. Vladisavljević GT, et al. (2013) Industrial lab-on-a-chip: Design, applications and scale-up for drug discovery and delivery. *Adv Drug Deliv Rev* 65:1626–1663.
34. Poiseuille JLM (1840) Recherches experimentales sur le mouvement des liquides dans les tubes es tres petits diameter. *C R Acad Sci* 11:961–967.
35. Kawakatsu T, et al. (2001) The effect of the hydrophobicity of microchannels and components in water and oil phases on droplet formation in microchannel water-in-oil emulsification. *Colloids Surf A Physicochem Eng Asp* 179:29–37.
36. Song H, Chen DL, Ismagilov RF (2006) Reactions in droplets in microfluidic channels. *Angew Chem Int Ed Engl* 45:7336–7356.



## Supplementary Information for

Wetting controls of droplet formation in step emulsification

Maximilian L. Eggersdorfer, Hansjörg Seybold, Alessandro Ofner, David A. Weitz and  
André R. Studart

André R. Studart

Email: andre.studart@mat.ethz.ch

### This PDF file includes:

Supplementary text

Figs. S1 to S5

Caption for movie S1

References for SI reference citations

### Other supplementary materials for this manuscript include the following:

Movie S1

## Theory

**Surface wetting compatibility condition.** The wetting compatibility condition is derived as follows: First, we approximate the cross section of the interface between the dispersed thread, the continuous phase and the top and bottom walls of the nozzle by circular arcs, as shown in Fig. 1 (front panel). At the triple point where the two phases meet with the nozzle surface the interface must form an angle of  $\alpha$  between the injected thread and the nozzle wall. Here  $\alpha$  is the contact angle measured from inside of the dispersed phase, Fig. 1 (front panel). Given these constraints, the radius of curvature of the interface is fully determined by the height  $h$  of the channel and the contact angle  $\alpha$ , namely  $R_n = -h/(2\cos(\alpha))$ . Consequently, if the neck width decreases below

$$w_{crit} = 2R_n \left(1 - \cos\left(\alpha - \frac{\pi}{2}\right)\right), \quad (1)$$

the left and right contact lines coincide and thus the condition  $R_n = -h/(2\cos(\alpha))$  cannot be obeyed anymore. Therefore, the thread detaches from the top and bottom walls of the nozzle triggering the Rayleigh-Plateau breakup. To measure  $w_{crit}$  experimentally and in the numerical simulations, we record the temporal evolution of the thread and measure the neck width over time (Fig. 2b). The time  $t_{crit}$  identifies the point in time, when the linear filling behavior changes to a power law collapse. Therefore,  $w_{crit}$  is given by the neck width  $w$  at  $t_{crit}$ . In the next step we calculate this transition point by intersecting the regression fits of the two corresponding regimes. Using the 95% confidence bounds of the fit parameters, also allows us to estimate an error bound for  $w_{crit}$  namely  $\Delta w_{crit} \approx 0.04h$ .

**Dripping to jetting transition.** Nearly monodisperse droplets are formed by dripping if the neck of the dispersed thread collapses in the nozzle via a Rayleigh-Plateau instability. The pinch-off is induced by the depletion of the dispersed phase from the nozzle. In this regime, the droplet size is independent of the flow rate of the continuous phase. Here, the flow of the dispersed phase is driven by the Laplace pressure difference between the thread in the shallow nozzle and the bulb forming in the deeper reservoir. A necessary condition for the neck to break-up in the nozzle is that it detaches from the walls triggering a Rayleigh-Plateau instability (see Fig. 2b). The neck width at the moment when the thread detaches from the walls is  $w_{crit}$ , as confirmed by experiments and simulations in Fig. 2b,c. For the neck width to shrink below  $w_{crit}$ , detach from the nozzle walls and trigger a Rayleigh-Plateau breakup, the flow of the dispersed phase out of the nozzle,  $Q_{out}$ , must be larger than the flow into the nozzle,  $Q_{in}$ . To estimate  $Q_{out}$  at the moment  $t_{crit}$ , we use the Laplace pressure difference between the thread in the channel and the bulb in the reservoir and the hydrodynamic resistance of the neck. The value of  $Q_{in}$  is known from the pump settings or can be estimated from the droplet formation frequency and droplet size averaged over dozens of droplets. In the case of  $Q_{out} < Q_{in}$  the neck does not decrease below the critical width  $w_{crit}$  and thus the bulb continues to grow. In this jetting regime, droplets are only formed when the bulb is sheared off by the continuous phase. Applying a simple mass balance for the flow configuration at the moment  $t_{crit}$  (Fig. 2a and Fig. S1) allows us to estimate the transition between dripping and jetting. The pressure at the neck,  $p_n$ , is given by:

$$p_n = p_0 + \gamma \left( \frac{1}{R_1} + \frac{1}{R_2} \right) \approx p_0 + \frac{2\gamma}{h} \cos(\pi - \alpha), \quad (2)$$

where  $R_1$  and  $R_2$  are the principal radii of the neck in the  $yz$ - and  $xy$ -plane, respectively. The other variables are the reference pressure in the reservoir,  $p_0$ , the surface tension between dispersed and continuous phase, the height of the shallow channel,  $h$ , and the contact angle  $\alpha$  of the dispersed phase with the channel walls. To make further progress, we apply the following simplifications in our model. First, we approximate the pressure of the continuous phase in the nozzle with the reference pressure  $p_0$  in the reservoir. This simplification is supported by our three-dimensional numerical simulations. Figure S2 shows the pressure field in the horizontal mid plane of the nozzle. The variation of the pressure in the continuous phase is considerably less than 10% of the pressure drop along the dispersed thread. Second, as the principal radius  $R_2$  is much larger than  $R_1$  we only consider the dominant curvature between the top and bottom walls of the device. Third we approximate the bulb by a sphere with radius  $R_d$ , which leads to:

$$p_d = p_0 + \frac{2\gamma}{R_d} \quad (3)$$

for the pressure  $p_d$  in the bulb. As mentioned before the flow into the bulb is driven by the pressure difference caused by the differences in interfacial curvature. Combining eq. 1, 2 and 3 we arrive at:

$$R_H Q_{out} = \left( \frac{2\gamma}{h} \cos(\pi - \alpha) - \frac{2\gamma}{R_d} \right), \quad (4)$$

where  $R_H$  is a hydrodynamic resistance. In the low flow limit, the minimal droplet diameter scales with  $R_d \sim 2h$  as shown in Fig. 4c. This allows us to simplify eq. 4 to:

$$R_H Q_{out} = [2 \cos(\pi - \alpha) - 1] \frac{\gamma}{h}. \quad (5)$$

The nozzle can only be depleted from the dispersed phase, if the flow out of the nozzle is higher than the refilling of the nozzle, thus:

$$Q_{in} < Q_{out} = [2 \cos(\pi - \alpha) - 1] \frac{\gamma}{h R_H}. \quad (6)$$

The hydrodynamic resistance is estimated from the geometry of the neck at time  $t_{crit}$ . Fig. S1a - c show the dispersed thread and a cross section through the neck together with the parabolic velocity profile of the dispersed phase, Fig. S1d. By approximating the neck geometry with a straight cylindrical channel with radius  $h/2$  and a length of order  $h$ , we arrive at:

$$Q_{in} < Q_{out} = (2 \cos(\pi - \alpha) - 1) \frac{\gamma \pi h^2}{128 \eta}. \quad (7)$$

Rearranging eq. (7) provides the condition for the transition from dripping to jetting as a function of the capillary number,  $Ca = u \cdot \eta / \gamma$  and the contact angle  $\alpha$ :

$$\frac{Q_{in} \eta}{h^2 \gamma} = Ca < [2 \cos(\pi - \alpha) - 1] \frac{\pi}{128}. \quad (8)$$

**Scaling of droplet diameter with contact angle.** The scaling of the droplet diameter with the contact angle can be derived in two ways, where the energy balance approach provides a functional description of the smallest possible drop diameters.

**Derivation of the droplet diameter scaling from the pressure drop.** During the dewetting process ( $t_b - t > t_{crit}$ ) the relative pressure drop  $\Delta p / p_d = [d \cdot \cos(\pi - \alpha) / 2h - 1]$

between the neck ( $p_n$ ) and the bulb ( $p_d$ ) is small ( $\approx 10^{-3}$ ) and does not vary considerably, Fig. S3. Thus, in a first approximation, it can be neglected arriving at  $0 = [d \cdot \cos(\pi - \alpha) / 2h - 1]$ . Solving this equation for the droplet diameter  $d$  yields  $d = 2h/\cos(\pi - \alpha)$ , which describes the proportionality of eq. (5) in the main text.

**Energy balance approach to derive the minimal droplet size for step emulsification.** To understand the effect of the wetting angle on the minimum size of droplets formed by dripping, one can also apply an energy balance approach similar to (1). Droplets only form spontaneously, if the total surface free energy after the break-up is lower than before. The difference in surface energy is calculated from the change in interfacial area as part of the volume of the dispersed phase in the nozzle is converted into a spherical drop. Initially the wedge-shaped nozzle is filled with the dispersed phase up to the step:

$$\Delta E = E_1 - E_2 - E_{drop} \geq 0, \quad (9)$$

where  $E_{drop}$  is the surface free energy of the drop and  $E_1$  and  $E_2$  are the free energy of the fluid thread inside the nozzle before and after the breakup, Fig. S4. The surface energy of the thread inside the nozzle can be estimated from the surface forces of the fluid with the nozzle walls and the interface between the two phases. Initially we have

$$E_1 = \gamma_{SD} (A_{top} + A_{bottom} + A_{left} + A_{right}) + \gamma_{CD} A_{front} = \gamma_{SD} (2A_{top} + 2A_{right}) + \gamma_{CD} A_{front}, \quad (10)$$

where  $\gamma_{SD}$  is the interfacial energy coefficient between the nozzle surface and dispersed phase and  $\gamma_{CD}$  is the interfacial energy coefficient between the dispersed and the continuous phase. Using the symmetry of the nozzle we arrive at

$$E_1 = 2\gamma_{SD} (A_{top} + A_{side}) + \gamma_{CD} A_{front}. \quad (11)$$

After the breakup the fluid volume of the thread is reduced by the volume of the drop:

$$\Delta V = wh = \pi \frac{d^3}{6}. \quad (12)$$

The surface energy of the remaining thread and the nozzle walls can be written as

$$E_2 = 2\gamma_{SD} (A'_{top} + A'_{side}) + \gamma_{CD} A'_{front}. \quad (13)$$

Here  $A'_{top}$  and  $A'_{side}$  are the new surface area components and the surface energy of a droplet with diameter  $d$  is given by

$$E_{drop} = \gamma_{CD} 4\pi d^2. \quad (14)$$

For simplicity we now neglect that the nozzle has a wedge shape and approximate the top and side surfaces of the nozzle by rectangles of width  $w$ , length  $L$  and height  $h$ . Thus, we arrive at

$$E_1 = \gamma_{SD} (2wL + 2Lh) + \gamma_{CD} wh. \quad (15)$$

Separating the volume of the thread which creates the final droplet reads as

$$E_2 = \gamma_{SD} [(2w(L-I)) + 2h(L-I)] + \gamma_{SC} [2wl + 2hl] + \gamma_{CD} wh. \quad (16)$$

In this case we can find a simple analytical expression for the surface area of the thread before and after the breakup. Using mass conservation for the droplet volume we find

$$I = \frac{\pi d^3}{6wh}, \quad (17)$$

and therefore

$$\begin{aligned}\Delta E &= E_1 - E_2 - E_{drop} = \gamma_{SD} (2wL + 2Lh) - \gamma_{SD} [(2w(L-l)) + 2h(L-l)] - \gamma_{SC} [2wl + 2hl] - \gamma_{CD} \pi d^2 \quad (18) \\ &= (\gamma_{SD} - \gamma_{SC}) 2wl + (\gamma_{SD} - \gamma_{SC}) 2hl - \gamma_{CD} \pi d^2 = (\gamma_{SD} - \gamma_{SC})(2wl + 2hl) - \gamma_{CD} \pi d^2\end{aligned}$$

Here  $l$  the distance of the fluid thread to the nozzle outlet after the breakup. Using the definition of the contact angle:

$$\gamma_{SD} - \gamma_{SC} = \gamma_{CD} \cos(\pi - \alpha), \quad (19)$$

and combining eq. 18 and 19 we arrive at:

$$\Delta E = \gamma_{CD} \cos(\pi - \alpha)(2wl + 2hl) - \gamma_{CD} \pi d^2 \geq 0. \quad (20)$$

Combining eq. 20 with eq. 17 finally gives an estimate of the smallest possible droplet diameter with  $\Delta E > 0$ :

$$\Delta E = \gamma_{CD} \cos(\pi - \alpha) \underbrace{\frac{w+h}{w \cdot h}}_{\substack{\text{specific wedge} \\ \text{surface area}}} - \gamma_{CD} \underbrace{\frac{6\pi d^2}{\pi d^3}}_{\substack{\text{specific droplet} \\ \text{surface area}}} \geq 0, \quad (21)$$

which finally results in an equation for the minimal droplet diameter

$$d_{min} = 3wh / [(w+h)\cos(\pi - \alpha)]. \quad (22)$$

Equation (22) shows that the minimal droplet diameter only depends on the nozzle geometry and the contact angle. As the contact angle decreases, so does the surface free energy of the wedge because the wedge area is weighted with  $\cos(\pi - \alpha)$ . This results in larger drops with reduced specific surface area.

**Simulations.** For all numerical simulations, we solve the time dependent three-dimensional Navier-Stokes equation using the Volume of Fluids (VOF) method. The interface between the dispersed and the continuous phase is captured using the geometric interface reconstruction scheme as implemented in the Ansys Fluent™ software v15 and v17. The computational mesh is created with OpenFOAM's blockMesh and exported to Fluent. The reservoir size is chosen to be approximately ten times larger than the horizontal nozzle width, so boundary effects are negligible. Figure S5 shows the nozzle geometry together with the horizontal cross section plane and the central symmetry axis of the nozzle. Fluid is injected into the nozzle through a velocity inlet which sets the inflow rate to  $Q_{in} = u \cdot A$ . Here  $A$  is the inlet cross section and  $u$  the inlet velocity. The nozzle walls are defined by no slip boundary conditions with a static contact angle imposed, thus approximating the dynamic process with a quasi-static boundary condition. This approximation may also be the cause for the instability of our simulations for contact angles close to the lower limit of  $\alpha = 2\pi/3$ . All other boundaries are kept open such that the fluid can freely flow out. The gauge pressure at the outlet is set to  $p \equiv 0$ . The capillary number is adjusted by changing surface tension  $\gamma$  and the inlet velocity  $u$  for constant viscosities of  $\mu_i = 1$  mPas and  $\mu_0 = 0.77$  mPas of the dispersed and continuous phases, respectively. Starting from a partly filled nozzle the equations of motions are integrated until a droplet is formed.

**Experiments.** The experiments are carried out in a glass device, which is produced through photolithography, HF etching and thermal bonding (2). A droplet maker consists of a whole array of nozzles each of which is 22 µm high with an angle of 10° and a length of 240 µm. The resulting width-to-height ratio is approximately 6.8±0.5. The microfluidic chip is connected with PTFE tubes via a Dolomite connector to syringes mounted on a Harvard Apparatus. A Fastcam Mini connected to a Leica microscope is used to record the experiments and the resulting images are analyzed with ImageJ for a single nozzle in the device. For the emulsification process, we mainly used oil-in-water (o/w) mixtures. Specifically, we used hexadecane, decane, dichloromethane, toluene, pentane, hexane, and chloroform as inner phase. Furthermore 2 wt-% of poly (vinyl alcohol) (MW = 31'000-50'000) are added to the continuous phase to stabilize the emulsion. When a hydrophobic surface is required to produce water-in-oil emulsions, a solution of 5 % octadecyltrimethoxysilane with 0.5 % butylamine in toluene is flushed through the device for 2 h. Water-in-oil emulsions are stabilized by adding 2 wt-% of polyglycerol polyricinoleate to the continuous phase.

To increase the hydrophilicity of the channels, the glass device is rinsed with a 1:80 polydiallyldimethylammonium chloride:water solution for 1 min, followed by water cleaning, and injection of an aqueous nanoparticle solution (Ludox colloidal silica, 22 nm 5 wt-% and silica, 100 nm 0.17 wt-%). To increase the hydrophobicity of the channels, the described nanoparticle treatment is used before silanizing the device as mentioned above.

Contact angle measurements are performed on a drop shape analyzer (DSA100, Krüss), where the dispersed phase is dripped onto a borofloat glass slide while surrounded by the continuous phase. Interfacial tension measurements are performed on a profile analysis tensiometer (PAT1, Sinterface Tech.), where droplets are measured in their relaxation mode.

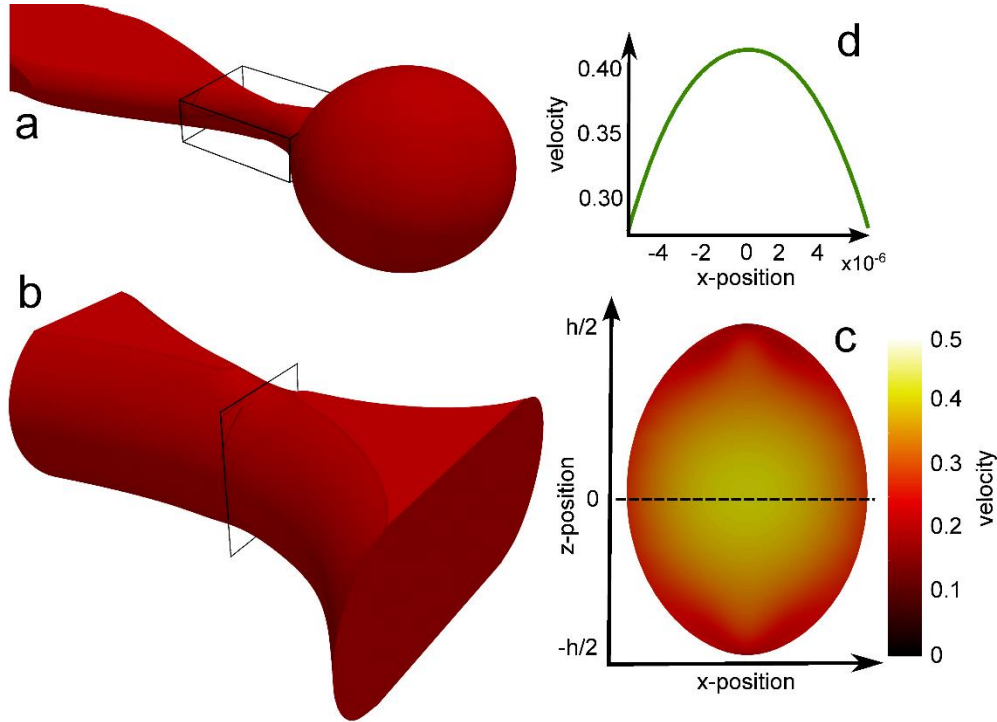


Fig. S1. a) Interface between the dispersed thread and the continuous phase at time  $t_{crit}$ , when the power law collapse of the neck is triggered. A mass balance is calculated for this configuration to estimate the dripping-to-jetting transition. (b) A close-up of the neck together with a cross section through the neck in (c). Colors indicate the magnitude of the flow velocity ranging from dark red ( $u = 0\text{m/s}$ ) to light yellow ( $u = 0.5\text{m/s}$ ). The velocity profile at  $z = 0$  through the dispersed neck is shown in (d). The simulation conditions are: contact angle  $\alpha = 150^\circ$ , surface tension  $\gamma = 0.02 \text{ N/m}$ , dispersed phase inlet velocity  $u = 0.085 \text{ m/s}$ , viscosity of dispersed phase  $\mu_i = 1 \text{ mPas}$ , viscosity of continuous phase  $\mu_o = 0.77 \text{ mPas}$ .

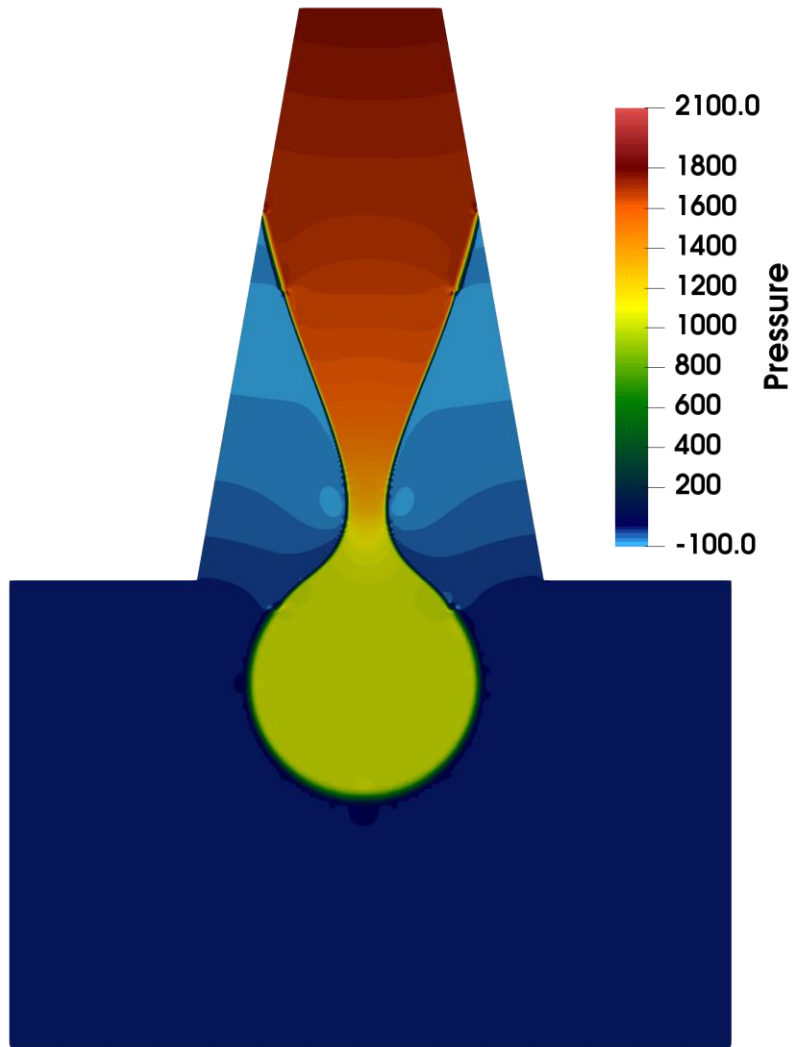


Fig. S2. Top view of the pressure field from three-dimensional numerical simulations at the moment when the neck detaches from the top and bottom walls. The continuous phase flows into the nozzle as the nozzle is depleted of the dispersed phase driven by the pressure gradient between the neck in the nozzle and the bulb in the reservoir. The simulation conditions are identical to Fig. S1.

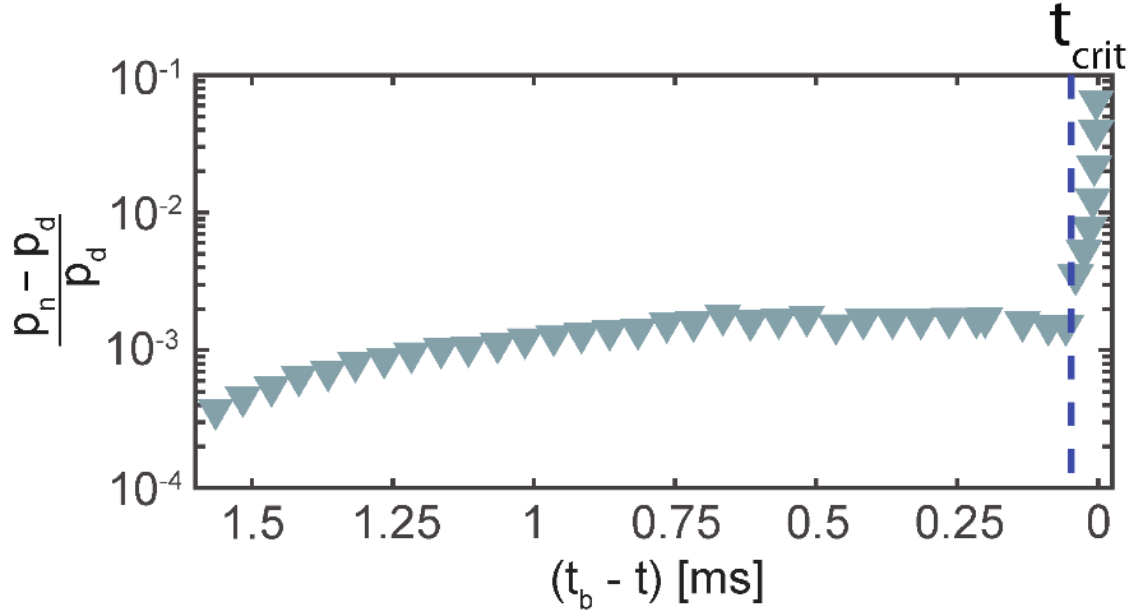


Fig. S3. Time evolution of the pressure drop  $\Delta p = p_n - p_d$  between the neck ( $p_n$ ) and the bulb ( $p_d$ ) non-dimensionalized by  $p_d$  extracted from three dimensional numerical simulations. During the wetting regime ( $t_b - t > t_{crit}$ ) the pressure drop remains almost constant at low values around  $10^{-3}$ . The Rayleigh-Plateau instability is triggered when the neck reaches the critical width  $w_{crit}$  at time  $t_{crit}$ . The collapse of the neck leads to an inflection point in the pressure profile as the neck pressure diverges during the Rayleigh-Plateau collapse.

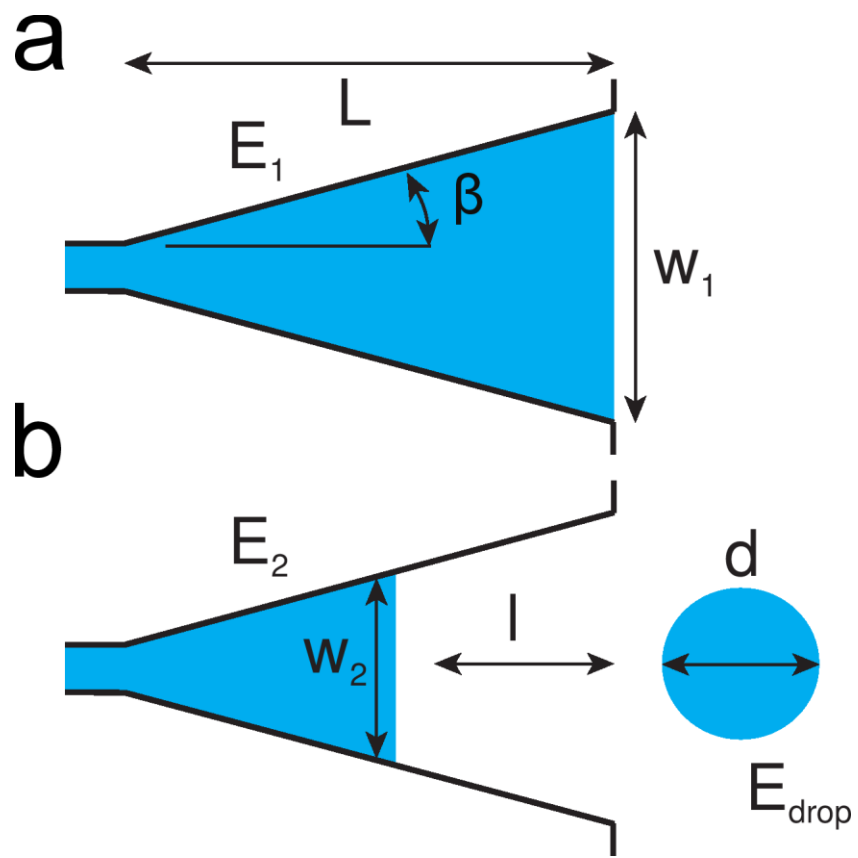


Fig. S4. Schematics of the liquid thread (blue) inside the nozzle before (a) and after the breakup (b).

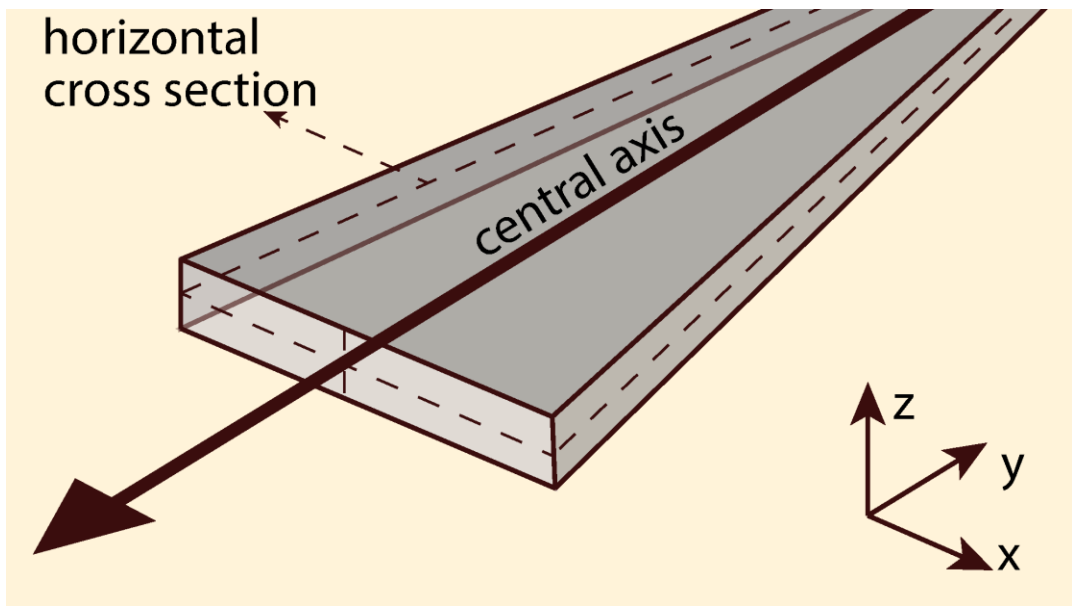


Fig. S5. Schematic view of the nozzle domain. Wall boundary conditions with non-zero contact angle are applied on the nozzle walls (gray). Outflow boundary conditions with zero pressure are applied on the reservoir boundaries. The dispersed fluid is injected via a velocity inlet. The horizontal plane marks the cross sections of Fig. 1(simulation, top) and Fig. 4a in the main text. The central symmetry axis along which we measured the simulated pressure profile is plotted with a black arrow.

## Movie S1

Droplet formation by dripping in a step-emulsification device for a Capillary number  $\text{Ca} \approx 6 \cdot 10^{-3}$ . The movie shows only the dispersed phase (red). The simulation conditions are: contact angle  $\alpha = 150^\circ$ , surface tension  $\gamma = 0.009 \text{ N/m}$ , dispersed phase inlet velocity  $u = 0.05 \text{ m/s}$ , viscosity of dispersed phase  $\mu_i = 1 \text{ mPas}$ , viscosity of continuous phase  $\mu_o = 0.77 \text{ mPas}$ .

## References

1. Li Z, Leshansky AM, Pismen LM, Tabeling P (2015) Step-emulsification in a microfluidic device. *Lab on a Chip* 15:1023–1031.
2. Ofner A, et al. (2016) High-Throughput Step Emulsification for the Production of Functional Materials Using a Glass Microfluidic Device. *Macromol Chem Phys* 218(2):1600472–10.